

# Microstructure of a Granular Amorphous Silica Ceramic Synthesized by Spark Plasma Sintering

Magnus Röding<sup>1,2,\*</sup>, Lorena A. Del Castillo<sup>1</sup>, Magnus Nydén<sup>3</sup>, and Bart Follink<sup>1,4</sup>

<sup>1</sup> Ian Wark Research Institute, University of South Australia, Mawson Lakes Campus, Adelaide, SA 5095, Australia.

<sup>2</sup> SP Food and Bioscience, Soft Materials Science, Box 5401, SE 402 29 Gteborg, Sweden.

<sup>3</sup> School of Energy and Resources, UCL Australia, University College London, 220 Victoria Square, Adelaide, SA 5000, Australia.

<sup>4</sup> School of Chemistry, Monash University, Clayton Campus, Melbourne, VIC 3800, Australia.

\* Corresponding author: SP Food and Bioscience, Soft Materials Science, Box 5401, SE 402 29 Gteborg, Sweden. Phone: +46 (0) 10 516 66 59. E-mail: magnus.rodning@sp.se.

We study the microstructure of a granular amorphous silica ceramic material synthesized by spark plasma sintering (SPS). Using monodisperse spherical silica particles as precursor, SPS yields a dense granular material with distinct granule boundaries. We use selective etching to obtain nanoscopic pores along the granule borders. We interrogate this highly interesting material structure by combining scanning electron microscopy (SEM), X-ray computed nanotomography (NanoCT), and simulations based on random close packed (RCP) spherical particles. We determine the degree of anisotropy caused by the uni-axial force applied during sintering, and our analysis shows

that our synthesis method provides a means to avoid significant granule growth and to fabricate a material with well-controlled microstructure.

**Keywords:** microstructure, nanoporous, scanning electron microscopy, sintering, X-ray computed tomography

# 1 Introduction

The effective macroscopic properties of a material are directly determined by its structure and properties on the microscopic scale. Thus, the design of functional materials begins with an understanding of small scale behavior (Torquato, 2002). Characterization of microstructure of a material has advanced substantially in recent years due to increasing capability of two- and three-dimensional imaging techniques and computational capacity for analysis of large, high-resolution data sets (Brandon and Kaplan, 2013). Fine structure such as granule boundaries and nanoscopic voids and pores can be directly imaged in granular materials.

Spark plasma sintering (SPS) is a method for compaction of granular materials used to synthesize a wide variety of dense solids including metals, plastics, composites, alloys, and ceramics. It has some interesting benefits over traditional sintering methods due to very fast heating and cooling rates and the potential to fabricate fully dense materials at comparatively low temperatures and to control granule growth. The kinetics of densification can be altered to design a range of different microstructures from the same precursor (Omori, 2000; Shen et al., 2002; Nygren and Shen, 2003; Munir et al., 2006). Thus, the resulting materials attract attention from a broad range of industries including minerals engineering and biotechnology due to their mechanical, thermodynamic, and transport properties (Kang, 2004). Although the physical driving force of compaction is essentially the decrease

of interfacial energy, sintering is a very complex process that is not easily modeled and understood (Munir et al., 2006; Chaim, 2007; Wang et al., 2010; German, 2010).

Considerable effort has been put into developing models for granular materials founded on spatial statistics and tessellations of space. For liquid foams, periodic tessellations can be traced back to Lord Kelvin (Thomson, 1887). In analogy to foams, we will refer to the 2D facets and 1D edges of granule boundaries as lamellae and borders, respectively. However, random tessellations such as Voronoi tessellations are more realistic models for random heterogeneous materials (Montminy et al., 2004; Redenbach, 2009; Kraynik et al., 2004), even though they do not correspond to an energy minimum (for example, no Voronoi tessellation in three dimensions can satisfy Plateau's laws that requires edges to meet at equal angles in random foams (Kraynik et al., 1999)) but are merely geometrical models. The sintering process can be thought of as a minimum-energy deformation of, typically, spherical particles such that the packing density approaches 1 and all voids between the spherical particles are filled. Hence, with an appropriate SPS process we can expect to obtain a dense granular material, consisting of approximately monodisperse, polyhedral particles, that is adequately modelled by space-filling particles based on random close packed (RCP) spherical particles (Lautensack et al., 2006).

In this work, we study the microstructure of a novel granular amorphous silica ceramic material synthesized by SPS. The precursors were spherical,

amorphous and homogenous in size ( $r = 0.75 \mu\text{m}$ ) and chemical composition as compared to another ceramic material prepared via SPS by Ramond et al. (2011), where the precursor (soda lime glass; also amorphous and spherical) were approximately 35 times bigger and were heterogeneous both in size and in chemical composition. SEM images of their soda lime glass samples sintered at temperatures above 522 °C show partial similarity to the microstructure of our sintered silica samples. In this study, we demonstrate that nanoscopic pores along the granule ('grain') borders can be obtained by selective etching. We combine scanning electron microscopy (SEM), X-ray computed nanotomography (NanoCT), and simulations to better understand this rather unique material. We determine the degree of anisotropy caused by the uni-axial force applied during SPS using SEM, and our analysis shows that our sintering method provides a means to avoid significant granule growth and hence allows fabrication of a material with well-controlled microstructure. We further study the pore structure using a combination of SEM, NanoCT and simulations to better understand the structure of this highly potential material.

## **2 Experimental**

### **2.1 Synthesis**

We synthesized the granular ceramic silica via SPS using the FDC SPS-925 unit (Fuji Electronic Industrial Co., Saitama, Japan). Monodisperse and

highly pure amorphous silica spheres ( $r = 0.75 \mu\text{m}$ , Geltech Inc., Jupiter, FL, US) were sintered under vacuum with a maximum pressure of 50 MPa, a sintering temperature of 1180 °C approached at first with a heating rate of 100 °C/min (which was then slowed down during the last 3 minutes of heating, to prevent temperature overshoot), and a dwell time of 5 min at the maximum temperature. The sintered disc was transparent. The borders of the constituent particles were then selectively etched by immersing the sintered silica in 20 % KOH solution heated to 60 °C, using two different etching times to obtain 150 nm and 450 nm pore diameters.

## **2.2 Scanning electron microscopy**

We obtained SEM images using a FEI Quanta 450 FEG (FEI, Hillsboro, OR, US) scanning electron microscope using 130 Pa chamber vacuum pressure and 30 kV accelerating voltage. The pixel size was 29.8 nm. Backscattered electron and secondary electron detector images were combined into a single image.

## **2.3 X-ray computed tomography**

We obtained the NanoCT images using a Zeiss NanoCT Ultra XRM-L200 Xradia (Zeiss, Jena, Germany) with a rotating copper anode as an x-ray source, operating with a photon energy of 8 keV. The voxel size was 16.2 nm and the theoretical resolution was 50 nm. Noise reduction was performed

using Gaussian smoothing with  $\sigma = 3$  voxels.

### 3 Results and discussion

After SPS, SEM (see Experimental) provides information on 2D cross-sections of the microstructure. SPS utilizes uni-axial force to compact the silica powder. By controlled fracturing of the sintered silica ceramic into pieces, we can select an image plane such that the axis of the applied force lies in that plane. Fig. 1 shows an example of an SEM image where the resulting anisotropy can be observed visually. We note that the near-polygonal 2D granule cross-sections are quite reminiscent of Voronoi tessellations. Interestingly, in striking analogy to foams, a closer look reveals that generally no more than three granule boundaries meet in the same point, and there are no visible pores so the material appears almost fully dense. However, we do observe a small number of quadruple nodes i.e. four granules meeting in the same point. These joints most probably point towards imperfections in the form of some residual pores. Notwithstanding our material being amorphous, the analogy with crystalline granular textures is striking. To avoid confusion with crystalline structures, we refrain from using the word 'grain' to describe the constituent particles, but to acknowledge the similarity, we use the similar word 'granule' throughout the text.

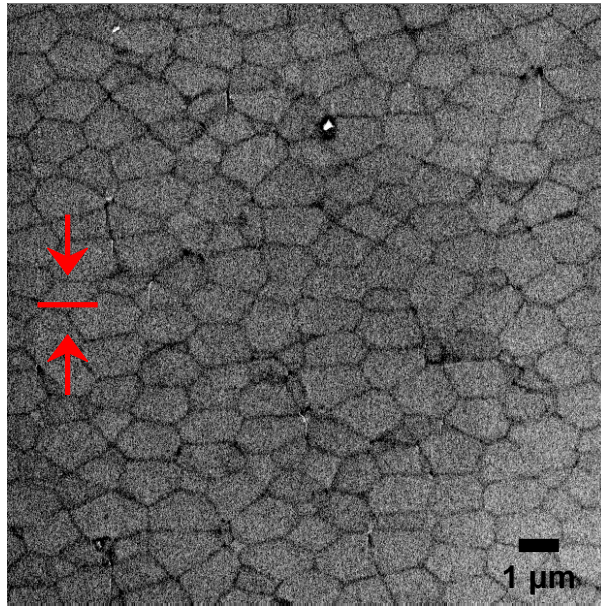


Figure 1: Example of an SEM image with field of view  $15\ \mu\text{m} \times 15\ \mu\text{m}$ . Some degree of anisotropy can be observed, caused by the uni-axial force applied during SPS. The angle of the applied force is (approximately) vertical in the image and indicated by the red arrows.

### 3.1 Microstructure simulation

We model the silica powder as random close packed (RCP) monodisperse ( $r = 0.75 \mu\text{m}$ ) spherical particles. A set of  $K = 10^4$  spherical particles are assigned random initial positions  $(x_k, y_k, z_k)$ ,  $k = 1, \dots, K$ , such that no two particles overlap (the minimum distance between any two center points is larger than  $2r$ ). A system energy

$$E = \sum_{k=1}^K (x_k^2 + y_k^2 + z_k^2) + E_{\text{overlap}}, \quad (1)$$

is defined, where  $E_{\text{overlap}}$  is  $\infty$  if any two particles overlap and 0 otherwise. The system energy is minimised using simulated annealing (Kirkpatrick et al., 1983). In each iteration, a randomly selected particle is assigned a normal distributed candidate displacement with standard deviation  $\sigma$ . If the displacement decreases the energy,  $\Delta E < 0$ , the new position is accepted. If the displacement increases the energy,  $\Delta E > 0$ , the new position is accepted only if

$$u \leq e^{-\Delta E/T(t)}, \quad (2)$$

where  $0 \leq u \leq 1$  is a uniform random number and  $T(t)$  is a time-dependent, exponentially decaying temperature. Simulated annealing is performed for nearly  $10^5$  epochs (complete loops over the entire set of particles) over 168 hours. The standard deviation of the random displacements is adapted so that the acceptance probability is kept in the range 0.2-0.4. The result of

Figure 2: (Color online) A realization of RCP of  $K = 10^4$  monodisperse spherical particles analogous to the silica powder precursor for SPS. The interior of this sphere cluster has packing density  $\phi \approx 0.644$ .

each simulation is a sphere cluster, the interior of which has packing density  $\phi \approx 0.644$ , well in accordance with known results for RCP of monodisperse spheres (Berryman, 1983; Jaeger and Nagel, 1992; Torquato et al., 2000; Song et al., 2008). Fig. 2 shows an example of an RCP configuration. Space-filling particles are obtained by performing a Voronoi tessellation (Aurenhammer, 1991) based on the RCP spherical particles, defining particle  $k$  as the set of all points  $(x, y, z)$  closer to the  $k$ th particle center  $(x_k, y_k, z_k)$  than to the  $l$ th particle center  $(x_l, y_l, z_l)$  for any  $l \neq k$ . In reality, the spherical particles are deformed but with constant volume  $V = 4\pi r^3/3$ , at least during the early stages of sintering, and the macroscopic volume of the material is reduced by a

factor  $\phi$ . However, the simulation generates particles with mean volume  $V/\phi$  and a slight 'artificial' polydispersity ( $\sigma/\mu \approx 0.04$ ) is introduced, originating from the fact that whereas the spherical particles are identical, the voids surrounding them are random in size. This polydispersity is immaterial since it corresponds roughly to the polydispersity of the silica particles used in the experiment). To ensure that the mean particle volume is  $V$ , the simulated microstructure is scaled by a factor  $\phi^{1/3}$  in each direction.

### 3.2 Anisotropy characterization

We take the uni-axial force during spark plasma sintering into account by modelling the microstructure of the ceramic as an anisotropic scaling of the simulated microstructure. The aim is to quantify the anisotropy from an SEM image. Let  $(x, y, z)$  be a coordinate system in which the image plane is  $(x, y, z_0)$  for some  $z_0$ . Because the anisotropy is the result of uni-axial force applied in some direction in the  $(x, y)$  plane, we wish to find a direction-dependent measure of scale to quantify direction and degree of anisotropy. Define another coordinate system  $(u, v, z)$  in which

$$\begin{aligned} u &= \cos(\theta)x + \sin(\theta)y \\ v &= -\sin(\theta)x + \cos(\theta)y \end{aligned} \tag{3}$$

where  $\theta$  is the angle of  $u$  relative to  $x$ . As a measure of scale, the standard deviation of the coordinates in the  $u$  direction comprising a granule cross-

section,  $\sigma_u(\theta)$ , can be used. Note that

$$\begin{aligned}
\sigma_u^2(\theta) &= \langle u^2 \rangle - \langle u \rangle^2 = \dots \\
&\cos^2(\theta) (\langle x^2 \rangle - \langle x \rangle^2) + \dots \\
&\sin^2(\theta) (\langle y^2 \rangle - \langle y \rangle^2) + \dots \\
&2 \cos(\theta) \sin(\theta) (\langle xy \rangle - \langle x \rangle \langle y \rangle), \tag{4}
\end{aligned}$$

where the moments are evaluated over all pixel coordinates comprising a granule cross-section. From the SEM image, granule cross-section contours ( $n = 380$ ) are manually identified from the raw image. Studying  $\sigma_u(\theta)$  for  $0 \leq \theta \leq \pi$ , it is found that the directions of largest and smallest average granule cross-section scale are near-orthogonal ( $1.55 \pm 0.01$ , approximately  $88.8^\circ$ ). This finding lends credence to the assumption that for some angle  $\theta = \theta_-$ ,  $u$  is the axis of the uni-axial force applied during sintering, i.e. the axis of maximum compression with scaling factor  $\rho_-$  and the  $v$  and  $z$  axes span the plane of maximum expansion with scaling factors  $\rho_+$ . The scaling factors are dependent on material and processing parameters and unknown, but two theoretical cases provide a hint of the bounds for these factors. In one theoretical extreme, compaction is perfectly isostatic and the resulting material is isotropic yielding  $\rho_- = \rho_+ = 1$ . In the other theoretical extreme compaction is due to uni-axial pressure and under certain hypothetical mechanical assumptions, each individual granule is on average compressed by the same factor as the macroscopic decrease in volume, i.e.  $\phi$ . Thus, we

postulate that we have the bounds

$$\begin{aligned} \phi &\leq \rho_- \leq 1 \\ 1 &\leq \rho_+ \leq \phi^{-1/2}. \end{aligned} \tag{5}$$

We estimate the parameter vector  $(\theta_-, \rho_-, \rho_+)$  from an SEM image using approximate Bayesian computation (Tavaré et al., 1997; Pritchard et al., 1999; Marjoram et al., 2003). A large number of microstructures are simulated as described above. Candidate samples  $(\theta_-^*, \rho_-^*, \rho_+^*)$  are generated from a flat prior distribution over a suitable range of parameter values. Simulated 2D cross-sections (field of view  $20 \mu\text{m} \times 20 \mu\text{m}$ ) similar to the SEM image are generated, scaled by the factors  $\rho_-^*$  and  $\rho_+^*$  in the coordinate system  $(u, v)$  defined by  $\theta_-^*$ . The similarity between the simulated and experimental images is defined by the criterion

$$C = \int_0^\pi \left( \langle \sigma_u^{\text{exp}}(\theta) \rangle - \langle \sigma_u^{\text{sim}}(\theta) \rangle \right)^2 d\theta, \tag{6}$$

where the averages are evaluated over all granule cross-sections in the experimental and simulated cross-sections. By keeping only those candidate parameters for which  $C \leq \epsilon$  for a threshold  $\epsilon$ , an approximate joint posterior distribution is obtained from which estimates for the individual parameters can be extracted. We obtain (m  $\pm$  sd)  $\theta_- = 1.42 \pm 0.05$  (approximately in the vertical direction in the SEM image),  $\rho_- = 0.89 \pm 0.02$ , and  $\theta_+ = 1.05 \pm 0.02$ .

Thus, the ratio of the experimental and simulated mean granule volumes is  $\rho_- \rho_+^2 = 0.98 \pm 0.05$ , indicating that no significant granule growth has occurred. Also, we note that the scaling factors were within the bounds postulated in Eq. (5). Fig. 3 shows the SEM image with the estimated axis of maximum compression indicated, an example of a simulated 2D cross-section with granule boundaries, the values of  $\langle \sigma_u^{\text{exp}}(\theta) \rangle$ , and the mean value of  $\langle \sigma_u^{\text{sim}}(\theta) \rangle$  for  $0 \leq \theta \leq \pi$ .

### 3.3 Pore structure characterization

As a means to understand the microstructure we perform highly selective etching of the granule borders to create a nanoporous material (see Experimental). First, we use SEM (see Experimental) to obtain 2.5D information about the pore structure where the pore diameter is approximately 150 nm. Fig. 4a clearly indicates a 3D pore structure. To get a better understanding of what is observed, we perform a simulation of an SEM image using the simulated microstructure. A few highly sophisticated algorithms for SEM simulation has been proposed, see e.g. (Drouin et al., 2007). We choose a simple phenomenological approach instead. A microstructure of  $5 \mu\text{m} \times 5 \mu\text{m} \times 2 \mu\text{m}$  is simulated. Etching is simulated by identifying voxels neighboring three particles simultaneously, and expanding the simulated pores to the appropriate diameter using a distance transform (Breu et al., 1995). Particles and pores are assigned 'densities'  $\delta_g$  and  $\delta_p$ . We assume that the 'diffusive' behaviour of the electrons results in a depth-dependent planar

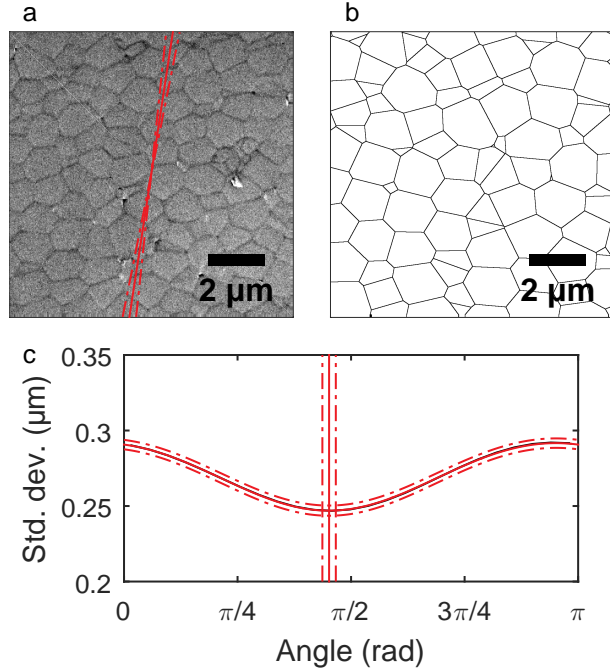


Figure 3: (Color online) Analysis of the microstructure anisotropy by evaluating direction-dependent standard deviations of granule cross-sections. In (a), an SEM image crop with field of view  $10 \mu\text{m} \times 10 \mu\text{m}$  from which granule cross-section boundaries ( $n = 380$ ) were manually identified together with the estimated axis of maximum compression (solid red line) with standard error bounds (dashed red lines) are shown. In (b), the granule boundaries of a corresponding cross-section with field of view  $10 \mu\text{m} \times 10 \mu\text{m}$  of a simulated microstructure are shown. In (c), the standard deviation of granule cross-sections as a function of angle for the experimental data (solid black line, almost occluded under solid red line), for the simulated data after anisotropic scaling (solid red line) with standard error bounds (dashed red lines), and the estimated angle of maximum compression (solid red vertical line) with standard error bounds (dashed red vertical lines) are shown.

Gaussian smoothing with standard deviation  $\sigma(z) = a + bz$  where  $z$  is the depth. Further, we assume that the contribution to the intensity is also depth-dependent and proportional to  $e^{-cz}$ . The intensity in each pixel of the simulated image is

$$I(x, y) = \int_{z=0}^{z_{\max}} (\mathbf{1}_g(x, y, z)\delta_g + (1 - \mathbf{1}_g(x, y, z))\delta_p) \times \dots e^{-cz} * f_G(x, y; 0, a + bz)dz + \epsilon(x, y), \quad (7)$$

where  $z_{\max} = 2 \mu\text{m}$ ,  $\mathbf{1}_g$  is the indicator function for a particle,  $f_G(x, y; 0, a + bz)$  is a Gaussian distribution, and  $\epsilon(x, y)$  is a Gaussian noise term. The parameters  $\delta_g$ ,  $\delta_p$ ,  $a$ ,  $b$ , and  $c$  were determined simply by visual inspection. Using this model, we manage to reproduce the SEM image with quite striking similarity given the simplicity of the approach, see Fig. 4b, providing a strong case for the physical nature of the microstructure. We also use NanoCT (see Experimental) for full 3D characterization of the pore structure. The thickness of the granule boundaries are in the order of the theoretical resolution of NanoCT (50 nm) so in an attempt to better resolve them we use a sample where the pore diameter is approximately 450 nm, see Fig. 5a-b. Although the theoretical resolution is sufficient, NanoCT provides limited contrast for this material. This renders the histogram of intensity values featureless, providing no guidance as to how to choose the threshold to binarize the image, see Fig. 5a. However, we try to circumvent the problem by calculating what the pore volume fraction should be using a simulated microstructure. By

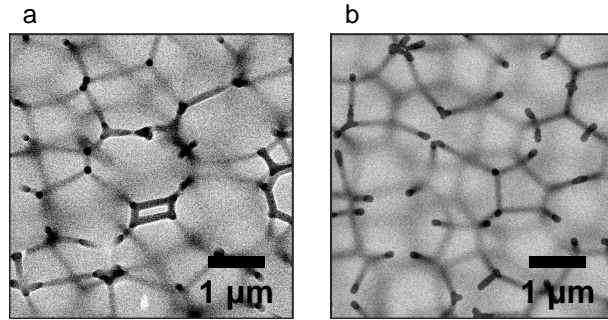


Figure 4: SEM analysis of the pore structure. In (a), an SEM image crop with field of view  $5 \mu\text{m} \times 5 \mu\text{m}$  is shown, where pores with 150 nm diameter are obtained with selective etching. In (b), a corresponding simulated SEM image with field of view  $5 \mu\text{m} \times 5 \mu\text{m}$  is shown. The striking similarity between the experimental and simulated SEM images further provides a strong case for the physical nature of the microstructure.

identifying the particle borders and expanding to the same pore diameter as in the real material, the simulated pore structure has a pore volume fraction of 0.26, see Fig. 5c. Finding the threshold corresponding to the same pore volume fraction in the experimental data gives a rough depiction of the real pore structure, see Fig. 5d-e (very small clusters of voxels have been removed from the identified structure in Fig. 5d). Unfortunately, we are forced to conclude that NanoCT cannot stand on its own as a quantitative technique for characterising this material.

## 4 Conclusion

We have studied the microstructure of a novel granular amorphous silica ceramic material. Spark plasma sintering of a monodisperse spherical silica

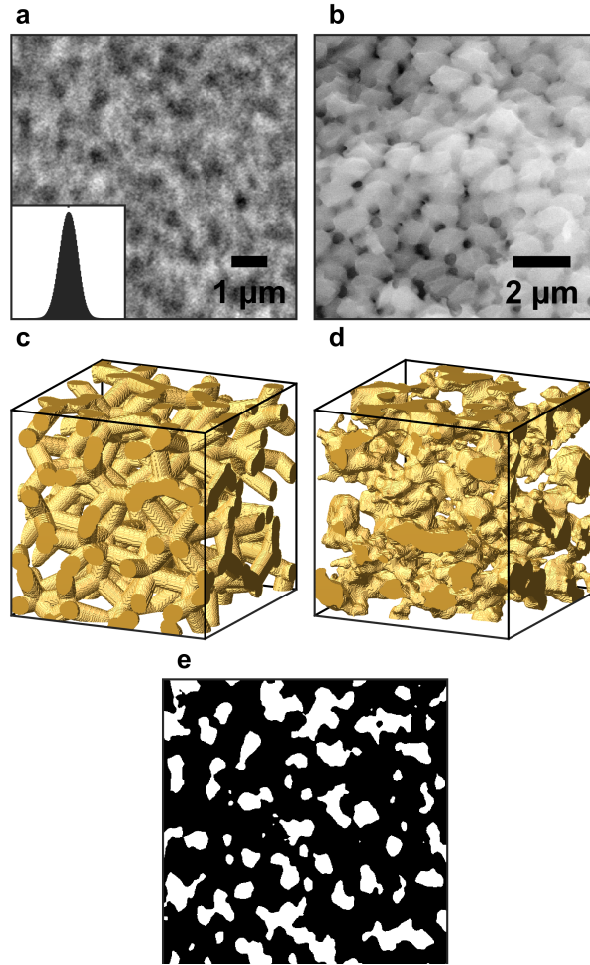


Figure 5: (Color online) 3D characterization of the pore structure using NanoCT. Pores with 450 nm diameter are obtained with selective etching. In (a), a slice of the raw NanoCT image with field of view  $8 \mu\text{m} \times 8 \mu\text{m}$  is shown. In the inset, the histogram of the intensity values is shown, providing no features and thus no guidance for selecting a threshold. In (b), an SEM image with field of view  $10 \mu\text{m} \times 10 \mu\text{m}$  that is used to estimate the pore diameter is shown. In (c), a simulated microstructure with field of view  $4 \mu\text{m} \times 4 \mu\text{m} \times 4 \mu\text{m}$  with the same pore diameter as the real material is shown. The pore volume fraction is 0.26. In (d), a NanoCT image of the microstructure with field of view  $4 \mu\text{m} \times 4 \mu\text{m} \times 4 \mu\text{m}$  is shown, picking the threshold for binarization such that the pore volume fraction is the same as that in the simulated microstructure in (c). In (e), a binarized version (white pores, black granules) of the same slice as in (a) is shown.

precursor yields a foam-like granular material with approximately polyhedral granules and well-defined granule boundaries. We demonstrate that selective etching of the granule borders can be used to fabricate a well-controlled nanoporous material. By combining SEM, NanoCT, and simulations, all of which jointly contribute to revealing different aspects of the characteristics, we have gained further insight into the microstructure of this highly promising material.

## Acknowledgements

Part of this work was performed at the South Australian node of the Australian National Fabrication Facility under the National Collaborative Research Infrastructure Strategy to provide nano- and micro-fabrication facilities for Australia's researchers.

## References

- S. Torquato. *Random heterogeneous materials: Microstructure and macroscopic properties*. Springer, 2002.
- D. Brandon and W.D. Kaplan. *Microstructural characterization of materials*. Wiley, 2013.
- M. Omori. Sintering, consolidation, reaction and crystal growth by the spark plasma system (SPS). *Mat. Sci. Eng. A*, 287:183–188, 2000.

- Z. Shen, M. Johnsson, Z. Zhao, and M. Nygren. Spark plasma sintering of alumina. *J. Am. Ceram. Soc.*, 85:1921–1927, 2002.
- M. Nygren and Z. Shen. On the preparation of bio-, nano- and structural ceramics and composites by spark plasma sintering. *Solid State Sci.*, 5: 125–131, 2003.
- Z.A. Munir, U. Anselmi-Tamburini, and M. Ohyanagi. The effect of electric field and pressure on the synthesis and consolidation of materials: A review of the spark plasma sintering method. *J. Mater. Sci.*, 41:763–777, 2006.
- S.-J.L. Kang. *Sintering: Densification, grain growth and microstructure*. Butterworth-Heinemann, 2004.
- R. Chaim. Densification mechanisms in spark plasma sintering of nanocrystalline ceramics. *Mat. Sci. Eng. A*, 443:25–32, 2007.
- C. Wang, L. Cheng, and Z. Zhao. FEM analysis of the temperature and stress distribution in spark plasma sintering: Modelling and experimental validation. *Comp. Mater. Sci.*, 49:351–362, 2010.
- R.M. German. Coarsening in sintering: Grain shape distribution, grain size distribution, and grain growth kinetics in solid-pore systems. *Crit. Rev. Solid State Mater. Sci.*, 35:263–305, 2010.
- W. Thomson. On the division of space with minimum partitional area. *Philos. Mag.*, 24:503–514, 1887.

- M.D. Montminy, A.R. Tannenbaum, and C.W. Macosko. The 3D structure of real polymer foams. *J. Colloid Interface Sci.*, 280:202–211, 2004.
- C. Redenbach. Microstructure models for cellular materials. *Comp. Mater. Sci.*, 44:1397–1407, 2009.
- A.M. Kraynik, D.A. Reinelt, and F. van Swol. Structure of random foam. *Phys. Rev. Lett.*, 93:208301, 2004.
- A.M. Kraynik, M.K. Neilsen, D.A. Reinelt, and W.E. Warren. Foam micromechanics: Structure and rheology of foams, emulsions, and cellular solids. In J.-F. Sadoc and N. Rivier, editors, *Foams and emulsions*, pages 259–286. Springer, 1999.
- C. Lautensack, K. Schladitz, and A. Särkkä. Modeling the microstructure of sintered copper. In *Proc. 6th Int. Conf. on Stereology, Spatial Statistics and Stochastic Geometry, Prague*, 2006.
- L. Ramond, G. Bernard-Granger, A. Addad, and C. Guizard. Sintering of soda-lime glass microspheres using spark plasma sintering. *Journal of the American Ceramic Society*, 94:2926–2932, 2011.
- S. Kirkpatrick, C.D. Gelatt, and M.P. Vecchi. Optimization by simulated annealing. *Science*, 220:671–680, 1983.
- J.G. Berryman. Random close packing of hard spheres and disks. *Phys. Rev. A*, 27:1053–1061, 1983.

- H.M. Jaeger and S.R. Nagel. Physics of the granular state. *Science*, 255: 1523–1531, 1992.
- S. Torquato, T.M. Truskett, and P.G. Debenedetti. Is random close packing of spheres well defined? *Phys. Rev. Lett.*, 84:2064–2067, 2000.
- C. Song, P. Wang, and H.A. Makse. A phase diagram for jammed matter. *Nature*, 453:629–632, 2008.
- F. Aurenhammer. Voronoi diagrams – a survey of a fundamental geometric data structure. *ACM Comput. Surv.*, 23:345–405, 1991.
- S. Tavaré, D.J. Balding, R.C. Griffiths, and P. Donnelly. Inferring coalescence times from DNA sequence data. *Genetics*, 145:505–518, 1997.
- J.K. Pritchard, M.T. Seielstad, A. Perez-Lezaun, and M.W. Feldman. Population growth of human Y chromosomes: A study of Y chromosome microsatellites. *Mol. Biol. Evol.*, 16:1791–1798, 1999.
- P. Marjoram, J. Molitor, V. Plagnol, and S. Tavaré. Markov chain Monte Carlo without likelihoods. *Proc. Natl. Acad. Sci.*, 100:15324–15328, 2003.
- D. Drouin, A.R. Couture, D. Joly, X. Tastet, V. Aimez, and R. Gauvin. CASINO V2.42 – A fast and easy-to-use modeling tool for scanning electron microscopy and microanalysis users. *Scanning*, 29:92–101, 2007.
- H. Breu, J. Gil, D. Kirkpatrick, and M. Werman. Linear time Euclidean

distance transform algorithms. *IEEE Trans. Pattern Anal. Mach. Intell.*,  
17:529–533, 1995.